Available online at www.sciencedirect.com
ScienceDirect
Trans. Nonferrous Met. Soc. China 34(2024) 3585−3598
Transactions of Nonferrous Metals Society of China
www.tnmsc.cn

Preparation, microstructure and degradation behavior of Mg−2Zn−0.4Sc−0.2Zr alloy wire

Yu-qing HE[1], Ri-chu WANG[1,2,3], Xiao-hui DUAN[4], Xiang PENG[1], Yu-si CHEN[1], Yan FENG[1,2,3]

1. School of Materials Science and Engineering, Central South University, Changsha 410083, China;
2. Key Laboratory of Electronic Packaging and Advanced Functional Materials of Hunan Province, Central South University, Changsha 410083, China;
3. National Key Laboratory of Science and Technology on High-strength Structural Materials, Central South University, Changsha 410083, China;
4. Department of Hepatobiliary Surgery, Human Provincial People's Hospital/ The First-affiliated Hospital of Hunan Normal University, Changsha 410005, China

Received 30 June 2024; accepted 21 October 2024

Abstract: A biodegradable Mg−2Zn−0.4Sc−0.2Zr (ZK20−0.4Sc) alloy wire with a diameter of 0.5 mm was prepared by a combination of hot extrusion and cold-drawing. The average grain size of ZK20−0.4Sc alloy wire on the longitudinal section along the drawing direction is approximately 7.3 μm. The texture results show relatively strong $\langle 11\bar{2}0\rangle$ and weak $\langle 10\bar{1}0\rangle$ fiber texture components parallel to the drawing direction. The ZK20−0.4Sc alloy wire exhibits better mechanical properties with the tensile strength, yield strength and elongate of (329±2) MPa, (287±2) MPa and (14.2±0.5)%, respectively. The better mechanical properties are mainly attributed to the grain refinement strengthening, dislocation strengthening and precipitation strengthening. With the immersion time increasing to 14 d, the corrosion type transfers from filament corrosion and pitting corrosion to severe localized corrosion.

Key words: Mg alloy wire; cold drawing; microstructure; mechanical properties; degradation behavior

1 Introduction

Magnesium (Mg) and its alloys have potential applications as biodegradation medical implants in the fields of cardiovascular, orthopedic and gastrointestinal because of the elastic modulus closer to that of human bone, good biodegradability and biocompatibility [1−5]. The use of biomedical Mg alloy wires has been explored as peripheral nerve repair, anastomosis nails and sutures [6−9]. Moreover, Mg and its alloy fine wires with diameters less than 0.5 mm can be knitted as tubular mesh stents or made as the reinforcement of polymer matrix composites for orthopedic surgery [10−12]. Mg and its alloys wires used as clinical implants have some requests. Firstly, the materials should keep adequate support strength after being implanted in the human body, and without obvious deformation during the internal service. Secondly, they should have good biosafety and biocompatibility, void inducing inflammation after implantation, and the degradation products are non-toxic to the human body. Thirdly, because of rapid degradation and its rate matching with the healing rate of the diseased tissue, the appropriate degradation rate will not cause premature loss of support for the implants [13−19].

Severe plastic deformation techniques, such as equal channel angular pressing (ECAP) and high-

Corresponding author: Yan FENG, E-mail: fengyanmse@csu.edu.cn
DOI: 10.1016/S1003-6326(24)66627-6

pressure torsion (HPT), have been used as the preparation of Mg and its alloy wires to refine the grain size or form specific texture [20−22]. However, the low productivity and the complexity limited their applications [23−28]. The common preparation methods of Mg alloy wire are extrusion and multi-pass drawing [29−34]. Compared with extrusion, drawing has obvious advantages. For example, it can obtain accurate dimension and can also be continuously fabricated at high speeds [35,36]. Drawing can be divided into cold drawing and hot drawing. The processing efficiency of hot drawing is high, and the Mg alloy wire produced has good ductility. But the low strength limits the requirements of implant materials. Cold drawing is carried out at room temperature, and the alloy wire tip is polished and directly drawn through the conical die to form. ZHENG et al [34] prepared a Mg−3Zn−0.2Ca medical Mg alloy wire with a diameter of 0.8 mm by extrusion and multi-pass cold drawing. Its grain size could be refined from 6.73 to 3.96 μm.

Adding low-alloying elements can effectively modify the microstructure and properties of Mg alloys [37,38]. In our previous study [39,40], adding a small amount of Sc element in Mg−2Zn−0.2Zr alloy refined grains, improved the strength and corrosion resistance of the alloy, and maintained good biocompatibility. It was found that the as-extruded Mg−2Zn−0.2Zr alloy containing 0.2% Sc displayed better corrosion resistance but lower mechanical properties [39]. However, with the increase of Sc content to 0.8%, the elongation significantly decreased and the degradation rate gradually increased. Considering the subsequent plastic deformation and degradation rate, Sc content should not be too high. Mg−2Zn−0.4Sc−0.2Zr (ZK20−0.4Sc) alloy with better plasticity was selected as the research object. Smelt, then homogenized annealing, hot extrusion, cold drawing and intermediate annealing were carried out to prepare a 0.5 mm diameter Mg alloy wire. When the accumulated deformation (0−31%) is small, ZK20−0.4Sc alloy can be directly cold-drawn plastic deformation. Because of frequently cutting off when large accumulated deformation exceeded 31% (diameter about 1 mm), ZK20−0.4Sc alloy wire was annealed at 250 °C for 0.5 h, and cold drawn with a single pass small deformation. Finally, ZK20−0.4Sc Mg alloy wire with a diameter of 0.5 mm (drawing deformation of 83%) was successfully prepared, and the microstructure and properties of ZK20−0.4Sc alloy wires were studied.

2 Experimental

The raw materials required for alloy smelting were high purity Mg (99.99%), high purity Zn (99.99%), Mg−30%Zr, and Mg−30%Sc intermediate alloys. The raw material was put into the tantalum crucible of the vacuum induction melting furnace in a target proportion of Mg−2Zn−0.4Sc−0.2Zr and heated until it was completely melted under the protection of argon gas. The melt was then poured into a stainless steel mold placed in the melting chamber and gradually cooled to room temperature to obtain a cylindrical ingot with a diameter of about 100 mm. The ingot was homogenized at 400 °C for 24 h to obtain a homogenized alloy with more uniform chemical composition and structure. The surface of the homogenized alloy was oxidized and removed to obtain a clean and smooth cylindrical casting blank. The cylindrical casting blank was preheated at 320 °C for 2 h, and the alloy was hot-extruded by a 300 t vertical extruder (the extrusion die was a round hole with a porous die at an extrusion rate of 5 mm/s). Then, the extruded bar with a diameter of 1.2 mm was obtained. The preparation process of Mg alloy wire and the illustration of the test direction and test surface of the sample are shown in Fig. 1. DD is the drawing direction, and RD is the radial direction. LS is the longitudinal section along DD, and TS is the cross section along RD. Considering the mechanical properties of Mg alloy, the cold drawing of single pass with small deformation and low speed was firstly carried out. The single pass deformation was controlled at 3%−5%, and the drawing rate was about 10 mm/s. The cumulative deformation of Mg alloy wire gradually increased after multiple cold drawing. When the diameter was deceased to 1 mm, frequent wire breakage occurred. Aiming to improve this situation, it is annealed in the heat treatment furnace at 250 °C for 0.5 h, and then gradually cold drawn to the wire with a diameter of 0.5 mm with the cumulative deformation of 83%. The diameter of the alloy wire and the cumulative drawing deformation (regarding the drawing deformation in the as-extruded state as zero) are shown in Table 1.

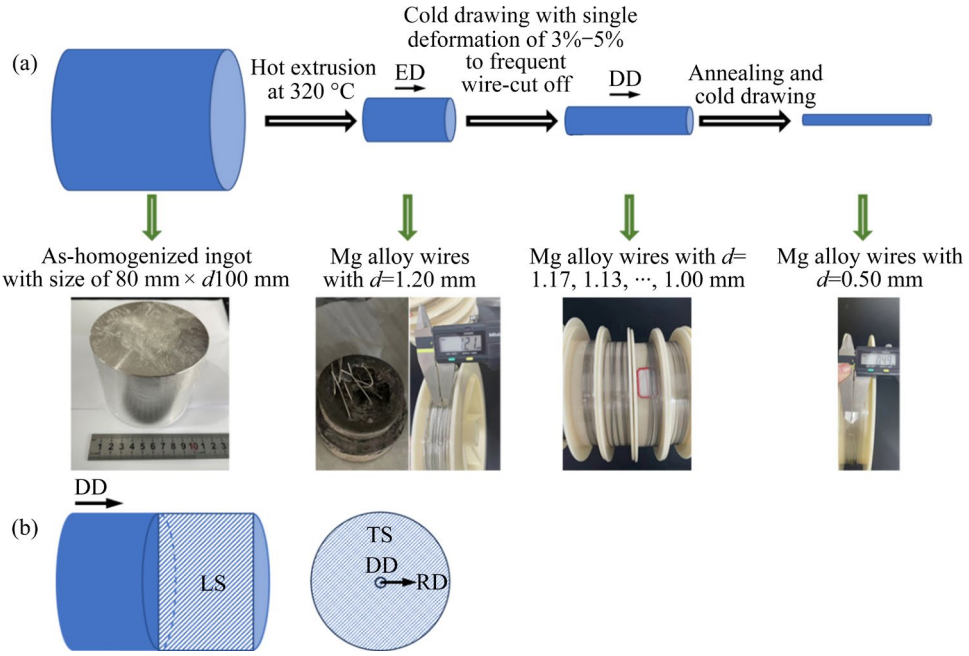

Fig. 1 Preparation technology (a), testing direction and section illustration (b) of ZK20−0.4Sc alloy wire

Table 1 Diameter and drawing reduction of as-extruded and as-drawn samples

Diameter/mm	Drawing reduction/%
1.20	0
1.17	5
1.13	11
1.00	31
0.50	83

The metallographic microscope (OM, Leica G20ST) was used to observe the microstructure of the alloy. The sample was mechanically ground step by step from 360# water abrasive sandpaper to 1600# metallographic sandpaper, and then mechanically polished using W0.5 diamond abrasive paste until there were no obvious scratches on the sample surface. A mixture solution of 92% (volume fraction) anhydrous ethanol and 8% (volume fraction) perchloric acid was prepared, and the solution temperature was reduced to about −30 °C with liquid nitrogen for electrolytic polishing. The surface of the obtained sample was smooth and bright without scratch. Then, it was corroded in the prepared metallographic etching solution (1 g oxalic acid + 1 mL nitric acid + 1 mL glacial acetic acid + 150 mL distilled water) for a period of time (the corrosion time of different components or states of the sample is different). Then, it was immediately washed with anhydrous alcohol to dry. The microstructure, phase, fracture and corrosion morphologies of the samples were observed by environmental scanning electron microscope (SEM, Quanta−200) using secondary electron (SE) and backscattered electron (BSE) images. The element contents of matrix, second phase and corrosion products were analyzed by energy dispersive spectrometer (EDS). The size and volume fraction of second phase were calculated with Image-Pro Plus (IPP) software according to the gray value difference between the second phase and the matrix. More than 4 SEM images were taken for calculations. The grain size was directly measured using IPP software. More than 4 OM images were taken for calculations. The microstructure and orientation were characterized by electron back scattering diffraction (EBSD, TESCAN MIRA4 LMH), and the obtained data were analyzed by HKL Channel 5 software. The microstructure was observed by transmission electron microscopy (TEM, Tecnai G2 F20 S-Twin) with the maximum accelerated voltage of 200 kV.

The tensile test at room temperature and the mechanical stability measurement of alloy wire along the drawing direction were performed using electronic universal testing machine (MTS−858) with a tensile rate of 1 mm/min. The mechanical stability testing was carried out as follows. The alloy wire was immersed in Hank's simulated body

fluid at 37 °C for 14 d. Then, its clamping end was inset with resin (diameter of 15 mm and length of both sides 30 mm), and the gauge segment of the alloy wire was about 25 mm in length. The alloy wire used for immersion test was cut into segments of about 50 mm in length, and the side of the alloy wire along the drawing direction was used as the main test surface. Three parallel samples of the same alloy were carried out to ensure the reliability of the experimental results. After immersion test, the alloy wire was put in chromic acid solution (180 g/L Cr_2O_3 water solution) by ultrasound for 5−8 min and in alcohol to remove the surface degradation products. Then, it was washed in ethanol for 5 min, finally dried with cold wind and the surface morphologies with different immersion time were observed using SEM.

3 Results and discussion

3.1 Microstructure

Figure 2 shows the SEM, OM and grain size distribution maps of ZK20−0.4Sc alloy wire. Irregular large-scale second phase and fine dispersed particles are distributed in the grains without obvious banded structure. The average size and the volume fraction of the second phases are approximately 0.02 μm and 3.83%, respectively. The corresponding EDS results of red areas in Fig. 2(a_2) are listed in Table 2. Large-scale irregular second phase mainly consists of Mg, Sc, Zn and Zr elements, considered as Mg(Zn,Sc,Zr) phase. As seen in Figs. 2(b_1, b_2), several twins appear in the alloy, and some large-scale irregular particles are

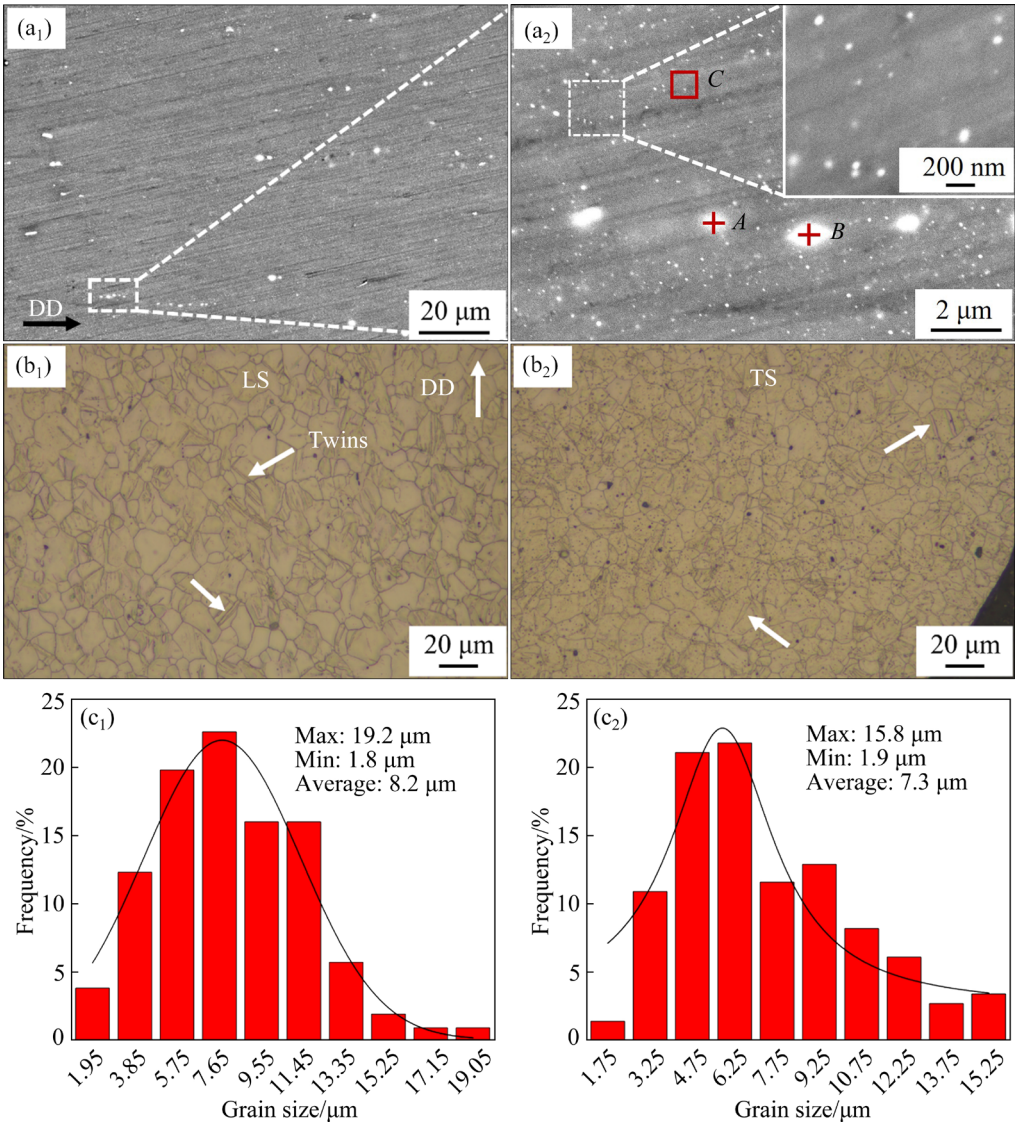

Fig. 2 SEM images (a_1, a_2), OM images on LS (b_1) and TS (b_2) planes and grain size distribution maps on LS (c_1) and TS (c_2) planes of ZK20−0.4Sc alloy wire

Table 2 EDS results of areas in Fig. 2

Area	Mg		Zn		Sc		Zr		Phase
	w/%	*x*/%	*w*/%	*x*/%	*w*/%	*x*/%	*w*/%	*x*/%	
A	86.10	95.03	4.82	1.98	1.06	0.63	8.02	2.36	Mg(Zn,Sc,Zr)
B	82.37	92.07	0.94	0.28	3.76	2.28	0.94	0.28	Mg(Zn,Sc,Zr)
C	95.07	98.16	12.92	5.37	0.84	0.47	1.79	0.49	α-Mg

w and *x* are mass fraction and molar fraction of atoms, respectively

distributed at the grain boundaries. The average grain sizes on the LS and TS planes are approximately 8.2 and 7.3 μm, respectively.

Figure 3 shows the TEM images of ZK20−0.4Sc alloy wire. Amounts of dislocation tangles and dislocation cells with a diameter of 200−300 nm are formed in the alloy wire. The subgrains with high dislocation pile-ups were possibly related to dislocation recovery during plastic deformation [33]. Some rod-like Mg(Zn,Sc,Zr) phases with the length of 30−110 nm and the width of 20−30 nm (marked as blue arrows) distributed within the grains. According to the invisible criterion of $\boldsymbol{g}\cdot\boldsymbol{b}=0$ ($\boldsymbol{g}$ is the diffraction vector and $\boldsymbol{b}$ is the Burgers vector), the visible dislocation component under $\boldsymbol{g}=0002$ condition is $\langle c\rangle$ dislocation component. In $\boldsymbol{g}=0002$ electron beam direction, $\langle c\rangle$ dislocation component is not visible, but in $\boldsymbol{g}=10\bar{1}0$ or $\boldsymbol{g}=11\bar{2}0$ condition there exists visible $\langle a\rangle$ dislocation. If the dislocations can be seen both under the $\boldsymbol{g}=0002$ and $\boldsymbol{g}=11\bar{2}0$ (or $\boldsymbol{g}=10\bar{1}0$), they are $\langle c+a\rangle$ mixture dislocations. Non-basal $\langle a\rangle$ dislocations can be visible only under $\boldsymbol{g}=10\bar{1}0$ or $\boldsymbol{g}=11\bar{2}0$ conditions along with their basal counterparts [41]. The magnified area *A* in Fig. 3(c) and the corresponding dark-field images (two-beam dark-field images) under $\boldsymbol{g}=0002$ and $\boldsymbol{g}=11\bar{2}0$ conditions are shown in Figs. 3(d−f). Amounts of dislocations (marked with green arrow) are illuminated under the $\boldsymbol{g}=11\bar{2}0$ condition but invisible under the $\boldsymbol{g}=0002$ condition, considered as $\langle a\rangle$ dislocations. Several curved and bowing $\langle c+a\rangle$ non-basal dislocations (marked as red dotted lines in Fig. 3(e) and red circles in Fig. 3(f)) are both under the $\boldsymbol{g}=0002$ and $\boldsymbol{g}=11\bar{2}0$ conditions. This indicates that the $\langle a\rangle$ and $\langle c+a\rangle$ non-basal slip systems are activated during the cold drawing and intermediate annealing process [42].

The grain orientation distribution map, KAM, recrystallization distribution, pole figure, and inverse pole figure (IPF) on longitudinal section (LS) of ZK20−0.4Sc alloy wire are shown in Fig. 4. As seen in Fig. 4(a), the large grain orientation distribution differences on the LS indicate no remarkable texture. According to Figs. 4(b) and (c), the large local misorientations are mainly concentrated in the deformed grains and sub-grains. The corresponding misorientation, local misorientation and recrystallization distribution maps are shown in Fig. 5. The frequency of low-angle grain boundary (LAGB, 2°−15°) and average KAM value are 30.2% and 1.37°, relatively. The frequencies of recrystallized, sub-structured and deformed grains in ZK20−0.4Sc alloy wire are 2.3%, 10.7% and 87.0%, respectively. This indicates higher contents of sub-structured and deformed grains than that of recrystallized grain. As seen in Fig. 4(d), {0001} basal and relatively weak $\{11\bar{2}0\}$ prismatic textures are presented in ZK20−0.4Sc alloy wire. As seen in Fig. 4(e), relatively strong $\langle 11\bar{2}0\rangle$ and weak $\langle 10\bar{1}0\rangle$ fiber texture components are paralleled to the drawing direction (//DD) are formed.

3.2 Mechanical properties

Tensile tests of the ZK20−0.4Sc alloy wire at room temperature were carried out and the stress−strain curve is shown in Fig. 6(a). The tensile strength (R_m), yield strength ($R_{0.2}$) and elongation (A) of the alloy wire are (329±2) MPa, (287±2) MPa and (14.2±0.5)%, respectively. Figure 6(b) shows the comparison of the mechanical properties with other Mg-based alloy in some references [10,34,43,44]. The ZK20−0.4Sc alloy wire has a higher tensile strength than that of most Mg-based alloy wire with a diameter of 0.5 mm, such as Mg0.8Ca, AX30 [43] and ZM21 [44]. The ZK20−0.4Sc alloy wire shows a remarkably higher elongation than ZEK100 [43] and Mg3Zn0.3Ca [34]. Figure 7 shows the fracture morphologies of ZK20−0.4Sc alloy wire. As seen in Fig. 7(a), the area of fracture surface is remarkably smaller than the original diameter of the wire, indicating an obvious necking in the tensile process.

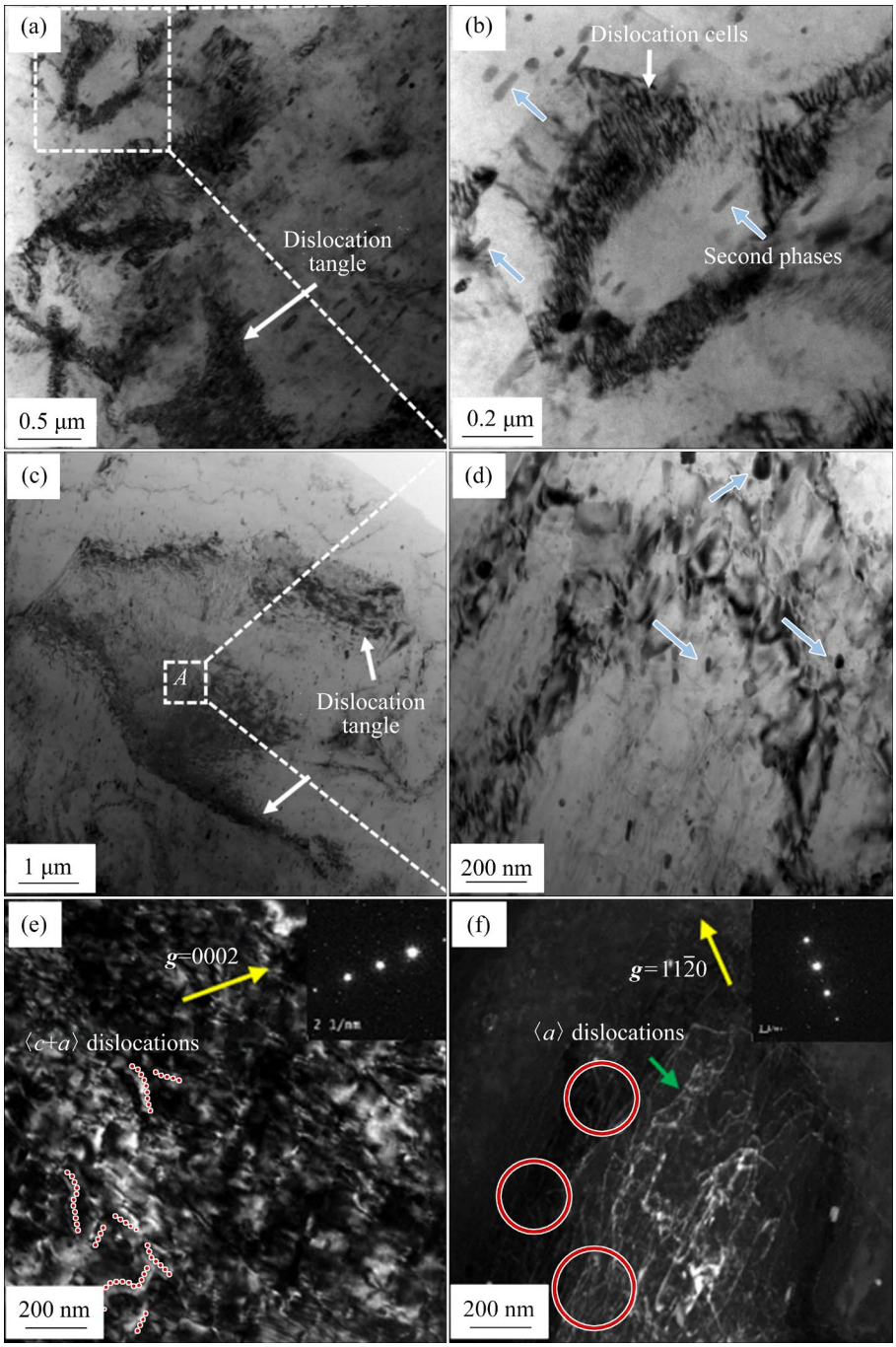

Fig. 3 TEM images of as-drawn ZK20−0.4Sc alloy wire: (a−d) Bright-field images; (e, f) Two-beam dark-field images under $\boldsymbol{g}$=0002 and $\boldsymbol{g}$=11$\bar{2}$0 conditions, respectively

Some dimples can be seen in Figs. 7(b, c), where some fine second phases are separated from the Mg matrix, displaying a ductile fracture. This phenomenon is mainly attributed to the elastic and plastic difference between the second phases and the matrix. The size of the dimples reflects the magnitude of the material's elongation. Amounts of small and deep dimples reflect higher ductility [45,46]. When the second phases are finer, the dimples are smaller. Therefore, the elongation of ZK20−0.6Sc alloy wire is relatively high.

The grain size, dislocation density and texture of alloy wire change before and after plastic deformation. These factors affect the mechanical properties of the alloy. Based on the Hall−Patch relationship, the increment of yield strength ($\Delta\tau_{GBS}$) because of the grain refinement effect can be calculated as follows [47,48]:

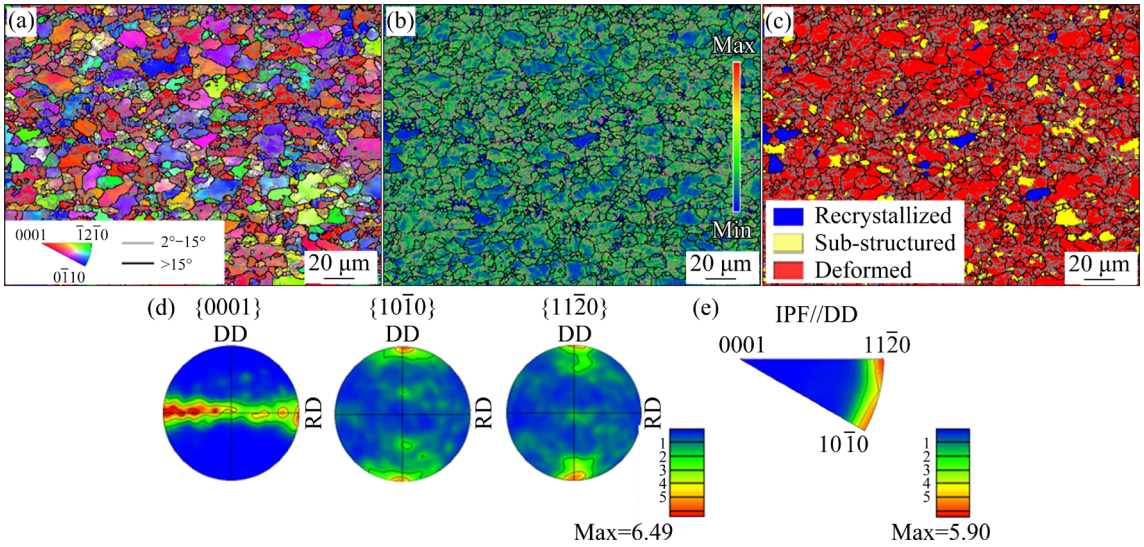

Fig. 4 Grain orientation distribution map (a), KAM (b), recrystallization distribution (c), pole figure (d), and inverse pole figure (e) of ZK20−0.4Sc alloy wire

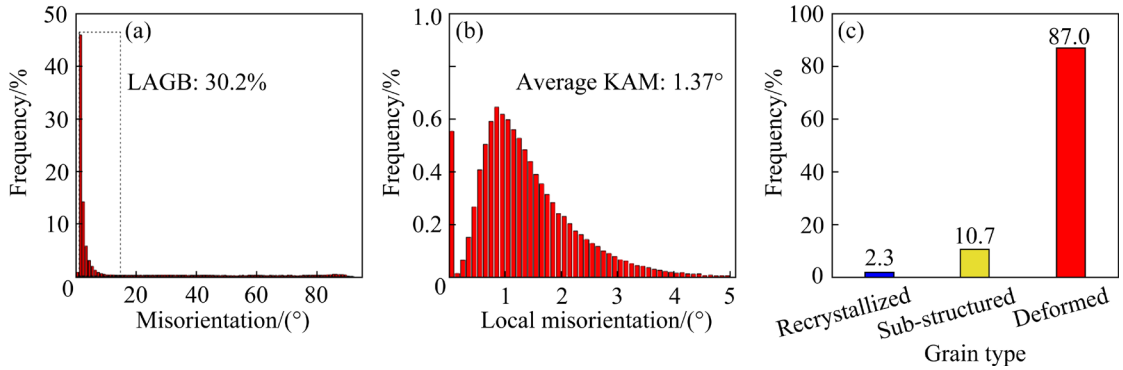

Fig. 5 Misorientation (a), local misorientation (b) and recrystallization distribution (c) maps of ZK20−0.4Sc alloy wire

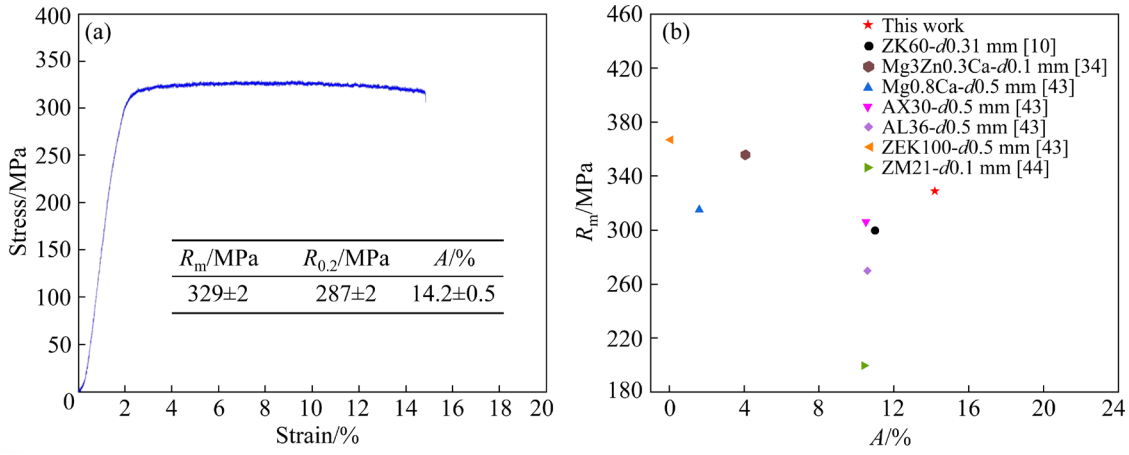

Fig. 6 Stress−strain curve of ZK20−0.4Sc alloy wire (a), and comparison of mechanical properties ZK20−0.4Sc alloy wire with various Mg alloy wires in some literatures (b)

$$\Delta\tau_{GBS}=Kd^{-1/2} \quad (1)$$

where K is the Hall−Petch coefficient (slope); d is the average grain size of the alloy. With the decrease of grain size, the yield strength of the alloy increases gradually. According to Fig. 2, the d values on the LS and TS planes are approximately 8.2 and 7.3 μm, respectively. Therefore, the contribution of grain refinement to the yield strength of ZK20−0.4Sc alloy wire on the TS and LS planes are 57 and 61 MPa, respectively.

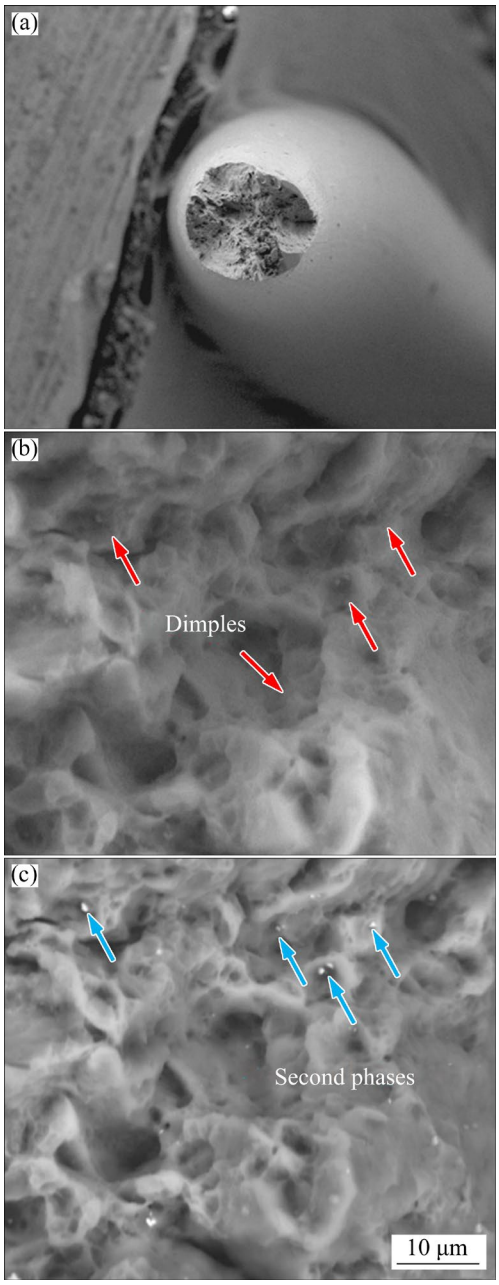

Fig. 7 Fracture morphologies of ZK20−0.4Sc alloy wire: (a, b) SE images; (c) BSE image

Secondly, a certain dislocation density is introduced into the alloy after extrusion and drawing. The contribution of dislocation strengthening ($\Delta\tau_{DS}$) can be expressed as follows [49]:

$$\Delta\tau_{DS}=\alpha MGb\rho^{1/2} \tag{2}$$

where α is a constant (0.2); M is the Taylor factor; G is the shear modulus (16.5 GPa); b is the amplitude of Burger vector (0.32 nm); ρ is the dislocation density. The geometric required dislocation density (ρ_{GNDs}) calculated from the average KAM value is expressed as follows [49]:

$$\rho_{GNDs}=2\theta/(\mu b) \tag{3}$$

where θ is the average KAM value (rad); μ is the scanning step set by EBSD measurement (μm). In Fig. 5(b), the θ value of ZK20−0.4Sc alloy wire is 1.37°, thus the dislocation density is 3.0×10^{-4} nm^{-2}. According to Eq. (2), the contribution value of dislocation strengthening ($\Delta\tau_{DS}$) is about 55 MPa. It can be seen that increasing the dislocation density will increase the yield strength of the alloy.

Combined with the microstructure of ZK20−0.4Sc alloy wire, precipitation strengthening has a significant effect. The precipitation strengthening contribution (τ_{PS}) because of the formation of Orowan loops around the second precipitates in Mg−Zn system alloy can be calculated as follows [40,50]:

$$\tau_{PS}=\frac{Gb}{2\pi\lambda\sqrt{(1-\upsilon)}}\ln\frac{d}{r_0} \tag{4}$$

where G is the shear modulus (≈16.6 GPa for Mg); υ is Poisson's ratio (≈0.33); d (nm) and λ (nm) are the mean particle diameter and the effective inter-particle spacing on the basal plane, respectively, r_0 (nm) is the core radius of dislocation (assume $r_0=|b|$). The mean particle diameter of the second precipitates is approximately 0.02 μm. The mean particle diameter can be computed as follows [51]:

$$\lambda=\sqrt{\frac{\pi}{\sqrt{3}f}}d \tag{5}$$

where f is the volume fraction of the precipitates, and the value is approximately 3.83%. According to the λ values, τ_{PS} of the second phases in ZK20−0.6Sc alloy wire is around 32 MPa.

Besides, the strength of Mg−Zn−Sc−Zr alloy can be improved by solid solution strengthening, and the contribution of solid solution effect ($\Delta\tau_{SS}$) can be expressed as follows [52,53]:

$$\Delta\tau_{SS}=kx^{2/3} \tag{6}$$

where k is a constant, and x is molar fraction of solid solution atom in the Mg matrix. According to Table 2, the molar fractions of Sc and Zr atoms in the Mg matrix are 0.47% and 0.49%, respectively. The solid strengthening effects of Sc and Zr atoms can be negligible. The molar fraction of Zn in the Mg matrix is 5.37%. Thus, the $\Delta\tau_{SS}$ value is calculated to be about 11 MPa. Therefore, the increase of mechanical properties of Mg−Zn−Sc−Zr alloy wires is mainly contributed to the grain

refinement strengthening, dislocation strengthening and precipitation strengthening.

Since biomedical implant materials such as biodegradable stents and anastomosis nails are made of Mg alloy wires, further examination of the formability of the alloy wire is required. Tensile test was carried out on the ZK20−0.4Sc alloy wire after tying (one knot). The tensile stress−strain curve and the macro fracture morphology are shown in Fig. 8. After tying a knot, the knot strength of the alloy wire is (163±12) MPa, and the elongation is (13.6±2.0)%. The fracture of the alloy wire is at the knot site (in Fig. 8(b)). The results show that ZK20−0.4Sc alloy wire has good formability and knotting strength as a potential biodegradable material. It meets the requirements of toughness for surgical sutures [54].

3.3 In vitro degradation behavior

Figure 9 shows the surface morphologies of ZK20−0.4Sc alloy wire immersed in the Hank's solution at 37 °C for different time. In the early immersion time of 7 d, a uniform degradation occurred on the alloy wire. During the following immersion time of 12 and 14 d, several corrosion pits are observed on the side of the alloy wire. After the immersion time of 14 d, its degradation rate calculated from the mass loss is D_m= (0.85±0.05) mm/a.

Figure 10 shows the surface morphologies after removing degradation products of ZK20−0.4Sc alloy wire immersed in Hank's solution at 37 °C for different time. Its corrosion type is mainly filament corrosion and pitting corrosion. The formation of filament corrosion is initiated at micro pits. The hydrolyzed and acidified filament head acts as the anode of the corroded filament, and the passivated filament tail as the cathode expands forward [55]. The filament corrosion occurred on various Mg and its alloys, such as pure Mg, AZ31 [56], Mg−3Zn [57], and AZ91 alloys [58]. These corrosion pits generally become the active corners of filament corrosion, and the Mg matrix as micro-anode is dissolved. This promotes the extension toward outside in the filament corrosion process. In the early immersion period, a slight pitting corrosion and a characteristic of filament corrosion with the width approximately 8 μm occur on the surface of the alloy wire. With the immersion time prolonging to 3 d, the width of filament corrosion enlarges to approximately 11 μm and the corrosion areas obviously increase. After the immersion time of 7 d, the corrosion surface of alloy wire is non-uniform. The filament width increases to approximately 40 μm and remarkable corrosion pits appear. The corrosion mechanism of pitting corrosion is mainly considered as selective adsorption of chloride ions (Cl^-) [59]. This phenomenon is also found in other Mg-based alloys [55,60−62]. After the immersion time of 14 d, the depth and areas of pitting corrosion further increase and the path of filament corrosion disappears. This displays severe localized corrosion. Moreover, as seen in Fig. 10(d_2), the corrosion depth between adjacent grains is different. That is, selective degradation of grains occurs. Overall, obvious uneven degradation occurs in the ZK20−0.4Sc alloy wire. It is mainly due to the introduction of defects such as dislocations during the cold drawing plastic deformation process. It makes the

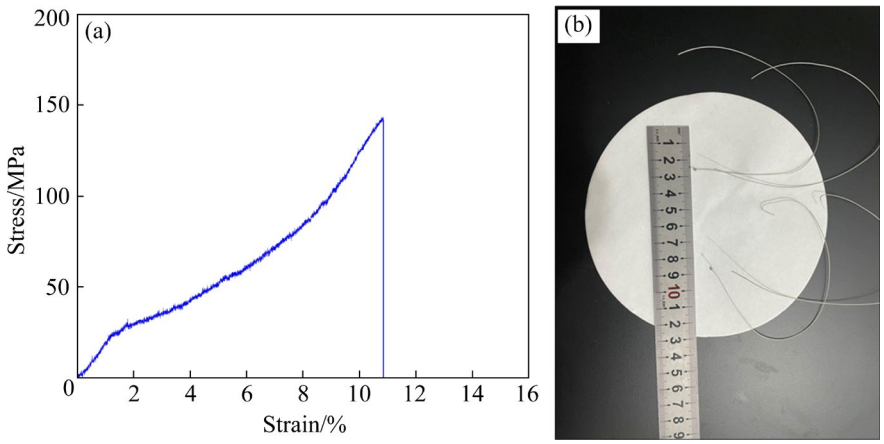

Fig. 8 Tensile tress−strain curve of ZK20−0.4Sc alloy wire after knotting (a), and its macro fracture morphology (b)

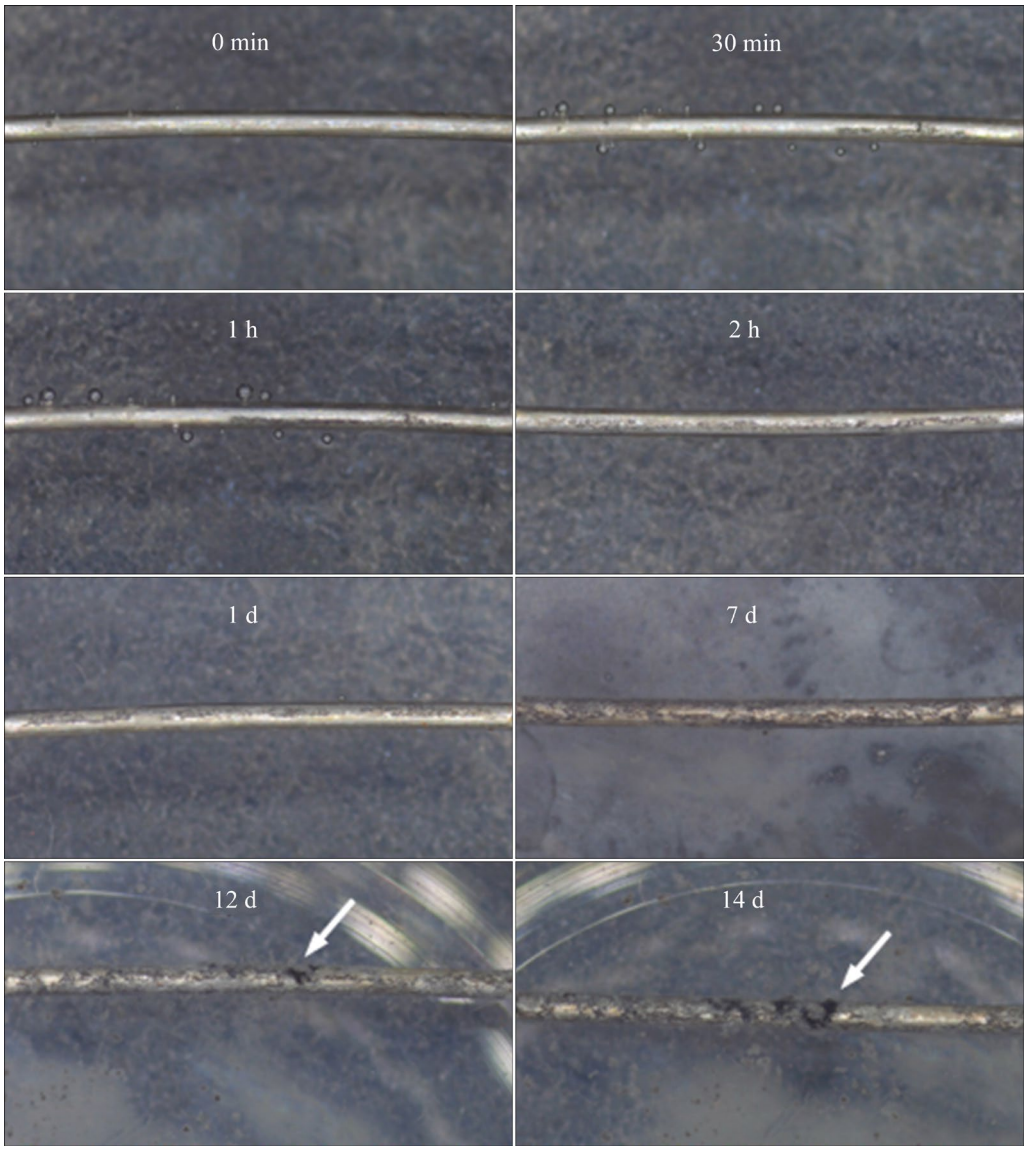

Fig. 9 Surface morphologies of ZK20−0.4Sc alloy wire immersed in Hank's solution at 37 °C for different time

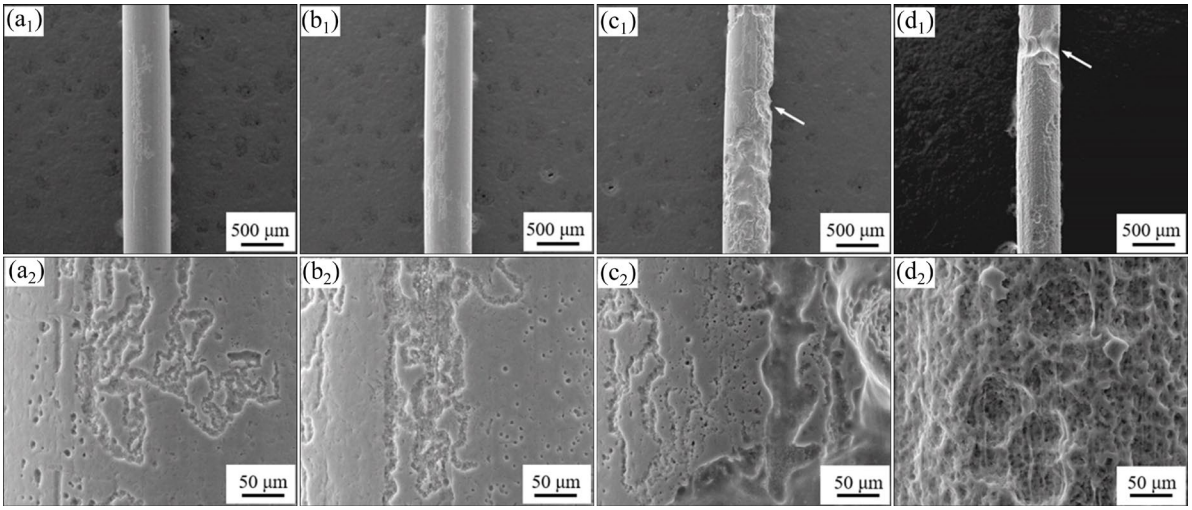

Fig. 10 Surface morphologies after removing degradation products of ZK20−0.4Sc alloy wire immersed in Hank's solution at 37 °C for different time: (a_1, a_2) 1 h; (b_1, b_2) 3 d; (c_1, c_2) 7 d; (d_1, d_2) 14 d

overall energy of the alloy wire unstable, and the chloride ions in the solution will preferably adsorb in the deformation area with high energy, thus leading to uneven degradation of the alloy wire and the following premature mechanical failure. A proper heat treatment is suggested to eliminate the residual stress generated in the drawing process to improve the comprehensive properties of the alloy wire.

4 Conclusions

(1) A novel biodegradable Mg−2Zn−0.4Sc−0.2Zr (ZK20−0.4Sc) alloy wire with a diameter of 0.5 mm is prepared by multi-pass cold drawing and annealing. Large-scale irregular Mg(Zn,Sc,Zr) second phase and fine particles are dispersedly distributed in the grains without obvious banded structure. The average size and the volume fraction of the second phases are approximately 0.02 μm and 3.83%, respectively.

(2) The weak {0001} basal texture and strong $\langle 11\bar{2}0\rangle$//DD fiber texture components are formed in ZK20−0.4Sc alloy wire. The ZK20−0.4Sc alloy wire is mainly composed of 2.3% recrystallized, 10.7% sub-structured and 87.0% deformed grains, with a large number of low angle grain boundaries.

(3) The tensile strength, yield strength and elongation of ZK20−0.4Sc alloy wire are (329±2) MPa, (287±2) MPa and (14.2±0.5)%, respectively. This is mainly attributed to the grain refinement strengthening, dislocation strengthening and precipitation strengthening. The relatively high elongation is relevant to the fine second phases.

(4) The main corrosion types of ZK20−0.4Sc alloy wire are filament corrosion and pitting corrosion. It is mainly due to the introduction of defects such as dislocations during the cold drawing plastic deformation process. Therefore, proper heat treatment is suggested to eliminate the residual stress generated in the drawing process to improve the comprehensive mechanical properties of the alloy wire.

CRediT authorship contribution statement

Yu-qing HE: Validation, Formal analysis, Investigation, Resources, Writing − Original draft, Writing − Review & editing; **Ri-chu WANG:** Methodology, Conceptualization, Formal analysis, Supervision, Project administration, Funding acquisition, Resources; **Xiao-hui DUAN**, **Xiang PENG** and **Yu-si CHEN:** Validation, Formal analysis − Review & editing; **Yan FENG:** Methodology, Conceptualization, Writing − Review & editing, Visualization, Supervision, Funding acquisition, Resources.

Declaration of competing interest

The authors declared that they have no conflicts of interest to this work and no financial and personal relationships with other people or organizations that can inappropriately influence this work. There is no professional or other personal interest of any nature or kind in any product, service and/or company that could be construed as influencing the position presented in, or the review of, the manuscript entitled.

Acknowledgments

The authors would like to thank for the financial support from the National Nature Science Foundation of China (No. 52274369), and the Hunan Provincial Natural Science Foundation, China (No. 2024JJ6521).

References

[1] ZHENG Y F, GU X N, WITTE F. Biodegradable metals [J]. Materials Science and Engineering R, 2014, 77: 1−34.

[2] YANG Yan, XIONG Xiao-ming, CHEN Jing, PENG Xiao-dong, CHEN Dao-lun, PAN Fu-sheng. Research advances in magnesium and magnesium alloys worldwide in 2020 [J]. Journal of Magnesium and Alloys, 2021, 9: 705−747.

[3] KIANI F, WEN C, LI Y C. Prospects and strategies for magnesium alloys as biodegradable implants from crystalline to bulk metallic glasses and composites—A review [J]. Acta Biomaterialia, 2020, 103: 1−23.

[4] JIANG Da-yue, DAI Yi-long, ZHANG Yu, YAN Yang, MA Jia-ji, LI Ding, YU Kun. Effects of heat treatment on microstructure, mechanical properties, corrosion resistance and cytotoxicity of ZM21 magnesium alloy as biomaterials [J]. Journal of Materials Engineering and Performance, 2018, 28: 33−43.

[5] GUI Zhen-zhen, KANG Zhi-xin, LI Yuan-yuan. Mechanical and corrosion properties of Mg−Gd−Zn−Zr−Mn biodegradable alloy by hot extrusion [J]. Journal of Alloys and Compounds, 2016, 685: 222−230.

[6] WITTE F. The history of biodegradable magnesium implants: A review [J]. Acta Biomaterialia, 2010, 6(5): 1680−1692.

[7] STAIGER M P, PIETAK A M, HUADMAI J, DIAS G. Magnesium and its alloys as orthopedic biomaterials: A review [J]. Biomaterials, 2006, 27(9): 1728−1734.

[8] VENNEMEYER J J, HOPKINS T, HERSHCOVITCH M, LITTLE K D, HAGEN M C, MINTEER D, HOM D B, MARRA K, PIXLEY S K. Initial observations on using magnesium metal in peripheral nerve repair [J]. Journal of Biomaterials Applications, 2014, 29(8): 1145−1154.

[9] SEITZ J M, DURISIN M, GOLDMAN J, DRELICH J W. Recent advances in biodegradable metals for medical sutures: A critical review [J]. Advanced Healthcare Materials, 2015, 4(13): 1915−1936.

[10] YAN Kai, SUN Jia-peng, BAI Jing, LIU Huan, WU Yu-na. Preparation of a high strength and high ductility Mg−6Zn alloy wire by combination of ECAP and hot drawing [J]. Materials Science and Engineering A, 2019, 739: 513−528.

[11] ZHANG Yue, CHEN Kai-yuan, LIU Huan, SHAO Yi, CHU Cheng-lin, XUE Feng, BAI Jing. A study of a biodegradable braided Mg stent for biliary reconstruction [J]. Journal of Materials Science, 2020, 55: 17170−17182.

[12] CAI Hong, ZHANG Yue, MENG Jiao, LI Xuan, XUE Feng, CHU Cheng-lin, TAO Li, BAI Jing. Enhanced fully-biodegradable Mg/PLA composite rod: Effect of surface modification of Mg−2Zn wire on the interfacial bonding [J]. Surface and Coatings Technology, 2018, 350: 722−731.

[13] DAI Yi-long, LIU Hui, TANG Yi-fu, XU Xue-mei, LONG Hai-tao, YAN Yang, LUO Zhen-hua, ZHANG Yu, YU Kun, ZHU Yong. A potential biodegradable Mg−Y−Ag implant with strengthened antimicrobial properties in orthopedic applications [J]. Metals, 2018, 8: 948−948.

[14] HE Yu-qing, WANG Ri-chu, PENG Chao-qun, FENG Yan, WANG Xiao-feng, CAI Zhi-yong. Microstructure, mechanical property, in vitro biodegradation behavior and biocompatibility of as-extruded Mg−2Zn−0.2Zr−*x*Nd (*x*=0.2, 0.6, 1.0) alloys [J]. Materials Characterization, 2023, 204: 113214.

[15] YANG Liu-zhong, FENG Yan, HE Yu-qing, YANG Lin-yi, LIU Han-chuan, WANG Xin-fa, PENG Chao-qun, WANG Ri-chu. Effect of Sc/Sm microalloying on microstructural and properties of Mg−2Zn−0.3Ca biodegradable alloy [J]. Journal of Alloys and Compounds, 2022, 907: 164533.

[16] YU Kun, DAI Yi-long, LUO Zhong-wei, LONG Hai-tao, ZENG Min, LI Zhao-hui, ZHU Jian-xi, CHENG Liang, ZHANG Yu, LIU Hui, ZHU Yong. In vitro and in vivo evaluation of novel biodegradable Mg−Ag−Y alloys for use as resorbable bone fixation implant [J]. Journal of Biomedical Materials Research (Part A), 2018, 106: 2059−2069.

[17] XIE Bin, ZHAO Ming-chun, XU Rong, ZHAO Ying-chao, YIN Deng-feng, GAO Cheng-de, ATRENS A. Biodegradation, antibacterial performance, and cyto-compatibility of a novel ZK30−Cu−Mn biomedical alloy produced by selective laser melting [J]. International Journal of Bioprinting, 2021, 7: 78−89.

[18] XIE Bin, ZHAO Ming-chun, TAO Jun-xi, ZHAO Ying-chao, YIN Deng-feng, GAO Cheng-de, SHUAI Ci-jun, ATRENS A. Comparison of the biodegradation of ZK30 subjected to solid solution treating and selective laser melting [J]. Journal of Materials Research and Technology, 2021, 10: 722−729.

[19] WANG Gao-qi, WANG Shou-ren, YANG Xue-feng, WEN Dao-sheng, GUO Yu. Microstructure, mechanical properties and fretting corrosion wear behavior of biomedical ZK60 Mg alloy treated by laser shock peening [J]. Transactions of Nonferrous Metals Society of China, 2023, 33: 1715−1728.

[20] JÄGER A, GÄRTNEROVA V, TESAŘ K. Microstructure and anisotropy of the mechanical properties in commercially pure titanium after equal channel angular pressing with back pressure at room temperature [J]. Materials Science and Engineering A, 2015, 644: 114−120.

[21] ZHANG C Z, ZHU S J, WANG L G, GUO R M, YUE G C, GUAN S K. Microstructures and degradation mechanism in simulated body fluid of biomedical Mg−Zn−Ca alloy processed by high pressure torsion [J]. Materials & Design, 2016, 96: 54−62.

[22] GAO Ming, ETIM I P, YANG Ke, TAN Li-li, MA Zheng. Enhancing mechanical property and corrosion resistance of Mg−Zn−Nd alloy wire by a combination of SPD techniques, extrusion and hot drawing [J]. Materials Science and Engineering A, 2022, 829: 142058.

[23] ALIHOSSEINI H, ZAEEM M A, DEHGHANI K. A cyclic forward−backward extrusion process as a novel severe plastic deformation for production of ultrafine grains materials [J]. Materials Letters, 2012, 68: 204−208.

[24] HAN Yu-xiang, CHEN Shu-yu, WAN Ying-chun, LIU Chu-ming, CHEN Zhi-yong. Microstructure, texture evolution and mechanical anisotropy of Mg−Gd−Y−Zn−Zr alloy sheets produced by unidirectional and cross rolling [J]. Materials Science and Engineering A, 2024, 893: 146127.

[25] WANG Jun-kai, LIU Chu-ming, JIANG Shu-nong, WAN Ying-chun, CHEN Zhi-yong. Effect of heat treatment on the microstructure and mechanical properties of a multidirectionally forged Mg−Gd−Y−Zn−Zr−Ag alloy [J]. Journal of Magnesium and Alloys, 2023, 11: 2042−2053.

[26] ZHANG Dong-dong, LIU Chu-ming, JIANG Shu-nong, GAO Yong-hao, WAN Ying-chun, CHEN Zhi-yong. Effects of extrusion process on microstructure, precipitates and mechanical properties of Mg−Gd−Y−Zr−Ag alloys [J]. Materials Science and Engineering A, 2022, 856: 143990.

[27] SHAO Jian-bo, CHEN Zhi-yong, CHEN Tao, WANG Ren-ke, LIU Yao-ling, LIU Chu-ming. Texture evolution, deformation mechanism and mechanical properties of the hot rolled Mg−Gd−Y−Zn−Zr alloy containing LPSO phase [J]. Materials Science and Engineering A, 2018, 731: 479−486.

[28] HUANG Ying-jie, LIU Chu-ming, JIANG Shu-nong, MA Ya-jie, WAN Ying-chun, CHEN Zhi-yong. Dislocation-induced β' precipitation behavior and strength−ductility synergistic enhancement in Mg−Gd−Y−Zr−Ag alloy [J]. Journal of Alloys and Compounds, 2023, 944: 169187.

[29] TESAŘ K, BALÍK K, SUCHARDA Z, JÄGER A. Direct extrusion of thin Mg wires for biomedical applications [J]. Transactions of Nonferrous Metals Society of China, 2020, 30: 373−381.

[30] ZUO J, NAKATA T, XU C, XIA Y P, SHI H L, WANG X J, TANG G Z, GAN W M, MAAWAD E, FAN G H, KAMADO S, GENG L. Effect of grain boundary segregation on microstructure and mechanical properties of ultra-fine grained Mg−Al−Ca−Mn alloy wires [J]. Materials Science and Engineering A, 2022, 848: 143423.

[31] SUN Liu-xia, BAI Jing, XUE Feng, TAO Li, CHU Cheng-lin, MENG Jiao. Exceptional texture evolution induced by multi-pass cold drawing of magnesium alloy [J]. Materials & Design, 2017, 135: 267−274.

[32] SUN Liu-xia, BAI Jing, YIN Ling-ling, GAN Yi-wei, XUE Feng, CHU Cheng-lin, YAN Jing-li, WAN Xiao-feng, DING Hong-yan, ZHOU Guang-hong. Effect of annealing on the microstructures and properties of cold drawn Mg alloy

wires [J]. Materials Science and Engineering A, 2015, 645: 181−187.

[33] CHEN W Z, ZHANG W C, CHAO H Y, ZHANG L X, WANG E D. Influence of large cold strain on the microstructural evolution for a magnesium alloy subjected to multi-pass cold drawing [J]. Materials Science and Engineering A, 2015, 623: 92−96.

[34] ZHENG Mao-bo, XU Guang-quan, LIU De-bao, ZHAO Yue, NING Bao-qun, CHEN Min-fang. Study on the microstructure, mechanical properties and corrosion behavior of Mg−Zn−Ca alloy wire for biomaterial application [J]. Journal of Materials Engineering and Performance, 2018, 27: 1837−1846.

[35] SAWAMIPHAKDI K, LAHOTI G D, GUNASEKERA J S, KARTIK R. Development of utility programs for a cold drawing process [J]. Journal of Materials Processing Technology, 1998, 80/81: 391−397.

[36] HADDI A, IMAD A, VEGA G. Analysis of temperature and speed effects on the drawing stress for improving the wire drawing process [J]. Materials & Design, 2011, 32: 4310−4315.

[37] LI Feng, CHENG Wei-li, YU Hui, WANG Hong-xia, NIU Xiao-feng, WANG Li-fei, LI Hang, HOU Hua. Corrosion behavior and mechanical properties of extruded low-alloyed Mg−0.5Bi−0.5Y−0.2Zn alloy [J]. Transactions of Nonferrous Metals Society of China, 2023, 33: 743−754.

[38] FAN Wen-xue, BAI Yu, LI Guang-yang, CHANG Xing-yang, HAO Hai. Enhanced mechanical properties and formability of hot-rolled Mg−Zn−Mn alloy by Ca and Sm alloying [J]. Transactions of Nonferrous Metals Society of China, 2022, 32: 1119−1132.

[39] HE Yu-qing, WANG Ri-chu, YANG Liu-zhong, YANG Lin-yi, LIU Han-chuan, WANG Xin-fa, PENG Chao-qun, FENG Yan. Influence of Sc on the microstructure, degradation behavior, biocompatibility in vitro and mechanical property of Mg−2Zn−0.2Zr alloy [J]. Materials & Design, 2022, 221: 110863.

[40] HE Yu-qing, WANG Ri-chu, PENG Chao-qun, FENG Yan, WANG Xiao-feng, CAI Zhi-yong. Influence of 0.6 wt.% Sc/Nd on the microstructure, mechanical property and in vitro biodegradation behavior of as-cast Mg−2Zn−0.2Zr alloy [J]. Journal of Alloys and Compounds, 2023, 942: 168890.

[41] ZHAO D X, MA X L, SRIVASTAVA A, TURNER G, KARAMAN I, XIE K Y. Significant disparity of non-basal dislocation activities in hot-rolled highly-textured Mg and Mg−3Al−1Zn alloy under tension [J]. Acta Materialia, 2021, 207: 116691.

[42] WEN Xiao-can, HUANG Hai-long, WU Hong-hui, ZHOU Mei-sa, BU Ye-qiang, YUAN Xiao-yuan, JIANG Sui-he, WANG Hui, LIU Xiong-jun, WANG Hong-tao, LIU Jia-bin, WU Yuan, LU Zhao-ping. Enhanced plastic deformation capacity in hexagonal-close-packed medium entropy alloys via facilitating cross slip [J]. Journal of Materials Science & Technology, 2023, 134: 1−10.

[43] SEITZ J M, FREYTAG P, BORMANN D, BACH F W. The manufacture of resorbable suture material from magnesium [J]. Advanced Engineering Materials, 2010, 12(11): 1099−1105.

[44] GRIEBEL A, SCHAFFER J. Cold-drawn ZM21 and WE43 wires exhibit exceptional strength and ductility [C]//Proceedings of the 6th Symposium on Biodegradable Metals. European Cells and Materials, 2014: 2.

[45] HOU L G, WANG T Z, WU R Z, ZHANG J H, ZHANG M L, DONG A P, SUN B D, BETSOFEN S, KRIT B. Microstructure and mechanical properties of Mg−5Li−1Al sheets prepared by accumulative rolling bonding [J]. Journal of Materials Science & Technology, 2018, 34(7): 317−323.

[46] SUN Yue-hua, WANG Ri-chu, REN Jian, PENG Chao-qun, CAI Zhi-yong. Microstructure, texture, and mechanical properties of as-extruded Mg−xLi−3Al−2Zn−0.2Zr alloys (x=5, 7, 8, 9, 11 wt.%) [J]. Materials Science and Engineering A, 2019, 755: 201−210.

[47] CACERES C H, MANN G E, GRIFFITHS J R. Grain size hardening in Mg and Mg−Zn solid solutions [J]. Metallurgical and Materials Transactions A, 2011, 42: 1950−1959.

[48] JIANG Xiang, HU Si-jia, WANG Li-min, LIU Xiao-hu, YANG Xu-yue, HUO Qing-huan. Unveiling the effect of Gd content on the dynamic recrystallization behavior and resultant mechanical property of magnesium [J]. Materials Science and Engineering A, 2023, 883: 145523.

[49] XU Yu-zhao, LI Jing-yuan, QI Ming-fan, LIAO Lu-hai, GAO Zhi-jun. Enhanced mechanical properties of Mg−Zn−Y−Zr alloy by low-speed indirect extrusion [J]. Journal of Materials Research and Technology, 2020, 9(5): 9856−9867.

[50] ALIZADEH R, LLORCA J. Interactions between basal dislocations and β'_1 precipitates in Mg−4Zn alloy: Mechanisms and strengthening [J]. Acta Materialia, 2020, 186: 475−486.

[51] NIE J F. Effects of precipitate shape and orientation on dispersion strengthening in magnesium alloys [J]. Scripta Materialia, 2003, 48: 1009−1015.

[52] WANG J Y, LI N, ALIZADEH R, MONCLÚS M A, CUI Y W, MOLINA-ALDAREGUÍA J M, LORCA J L. Effect of solute content and temperature on the deformation mechanisms and critical resolved shear stress in Mg−Al and Mg−Zn alloys[J]. Acta Materialia, 2019, 170: 155−165.

[53] MA Ya-jie, LIU Chu-ming, HUANG Ying-jie, JIANG Shu-nong, GAO Yong-hao, WAN Ying-chun, CHEN Zhi-yong. Effect of extrusion parameters on microstructure, mechanical properties and damping capacities of Mg−Y−Zn−Zr alloy [J]. Journal of Alloys and Compounds, 2023, 935: 168122.

[54] ZHENG Yu-feng, QIN Ling, YANG Ke. Degradable metals [M]. Beijing: Science Press, 2016. (in Chinese)

[55] SONG Ying-wei, SHAN Da-yong, CHEN Rong-shi, HAN En-hou. Corrosion characterization of Mg−8Li alloy in NaCl solution [J]. Corrosion Science, 2009, 51(5): 1087−1094.

[56] HARA N, KOBAYASHI Y, KAGAYA D, AKAO N. Formation and breakdown of surface films on magnesium and its alloys in aqueous solutions [J]. Corrosion Science, 2007, 49(1): 166−175.

[57] WANG Hong-xin. In-situ study on the dynamic growth process of filiform corrosion on magnesium alloys [D]. Shenyang: Shenyang University of Technology, 2017. (in Chinese)

[58] LUNDER O, LEIN J E, HSJEVIK S M, AUNE T K. Corrosion morphologies on magnesium alloy AZ91 [J]. Materials and Corrosion, 1994, 45: 331−340.
[59] GAO Li-li, ZHANG Chun-hong, ZHANG Mi-lin, HUANG Xiao-mei, SHENG Nan. The corrosion of a novel Mg−11Li−3Al−0.5RE alloy in alkaline NaCl solution [J]. Journal of Alloys and Compounds, 2009, 468(1/2): 285−289.
[60] XIANG Qing, JIANG Bin, ZHANG Yu-xin, CHEN Xiao-bo, SONG Jiang-feng, XU Jun-yao, FANG Liang, PAN Fu-sheng. Effect of rolling-induced microstructure on corrosion behaviour of an as-extruded Mg−5Li−1Al alloy sheet [J]. Corrosion Science, 2017, 119: 14−22.
[61] SUN Yue-hua, WANG Ri-chu, PENG Chao-qun, CAI Zhi-yong. Microstructure and corrosion behavior of as-extruded Mg−*x*Li−3Al−2Zn−0.2Zr alloys (*x*=5, 8, 11 wt.%) [J]. Corrosion Science, 2020, 167: 108487.
[62] SUN Yue-hua, WANG Ri-chu, PENG Chao-qun, WANG Xiao-feng. Microstructure and corrosion behavior of as-homogenized Mg−*x*Li−3Al−2Zn−0.2Zr alloys (*x*=5, 8, 11 wt.%) [J]. Materials Characterization, 2020, 159: 110031.

Mg−2Zn−0.4Sc−0.2Zr 合金丝的制备、显微组织及降解行为

贺玉卿[1]，王日初[1,2,3]，段小辉[4]，彭 翔[1]，陈于思[1]，冯 艳[1,2,3]

1. 中南大学 材料科学与工程学院，长沙 410083；
2. 中南大学 电子封装与先进功能材料湖南省重点实验室，长沙 410083；
3. 中南大学 高强度结构材料科学技术国家重点实验室，长沙 410083；
4. 湖南省人民医院/湖南师范大学第一附属医院 肝胆外科，长沙 410005

摘 要：采用热挤压和冷拔相结合的方法制备直径为 0.5 mm 的可生物降解 Mg−2Zn−0.4Sc−0.2Zr (ZK20−0.4Sc)合金丝。ZK20−0.4Sc 合金丝沿拉伸方向纵截面的平均晶粒尺寸约为 7.3 μm。织构结果显示，平行于拉伸方向形成较强的⟨11$\bar{2}$0⟩和较弱的⟨10$\bar{1}$0⟩纤维织构组分。该合金丝具有较优的力学性能，其抗拉强度为(329±2) MPa，屈服强度为(287±2) MPa，伸长率为(14.2±0.5)%。其较优的力学性能主要归因于细晶强化、位错强化和析出强化。随着浸泡时间增加至 14 d，该合金丝的腐蚀类型由丝状腐蚀和点蚀转变为严重的局部腐蚀。

关键词：镁合金丝；冷拉拔；显微组织；力学性能；降解行为

(Edited by Wei-ping CHEN)